CHALMERS
UNIVERSITY OF TECHNOLOGY

NUMERICAL PREDICTION OF ROLLING CONTACT FATIGUE CRACK GROWTH IN A RAILHEAD

12th International Conference on Contact Mechanics and Wear of Rail/Wheel Systems (CM2022), Melbourne, Australia, 4-7 September 2022

NUMERICAL PREDICTION OF ROLLING CONTACT FATIGUE CRACK GROWTH IN A RAILHEAD

Mohammad Salahi Nezhad [1,*], Fredrik Larsson [1], Elena Kabo [2], Anders Ekberg [2]

[1] CHARMEC / Department of Industrial and Materials Science, Chalmers University of Technology, SE-412 96 Gothenburg, SWEDEN
[2] CHARMEC / Department of Mechanics and Maritime Sciences, Chalmers University of Technology, SE-412 96 Gothenburg, SWEDEN

[*] E-mail: salahi@chalmers.se

Abstract: The influence of crack face friction on predicted crack paths in a 2D rail model is investigated numerically. A surface-breaking inclined rolling contact fatigue crack is propagated under a moving contact load, combined thermal and contact load, and combined (rail) bending and contact. Coulomb crack face friction is included. The growth direction is predicted using an accumulated vector crack tip displacement criterion. Frictional cracks are found to grow deeper into the rail under pure contact load and combined bending and contact while friction has a moderate influence under combined thermal and contact loads. Furthermore, friction reduces crack growth rates.

Keywords: Crack face friction; Rolling contact fatigue; Crack growth direction; Vector crack tip displacement; Crack propagation; Finite element modeling.

1. Introduction

Rolling Contact Fatigue (RCF) treatment is an inevitable and expensive part of the maintenance of railway tracks due to the potential safety implications [1]. Costs and risk magnitudes are largely governed by the depth of propagation of such cracks – shallow cracks result in limited material fall-out, and require moderate surface reprofiling through grinding or milling, whereas deeper cracks cause deeper material fall-out or transverse fracture, which requires heavy reprofiling or rail replacement. The main motivation for the current study is to be able to predict how operational conditions influence the propensity for deeper and transverse growth. Since the ability for tests is limited due to scaling issues and the requirements for complex and timely tests, this requires the development of a reliable numerical framework and predictive models. In previous studies [2, 3] such a predictive framework has been developed and verified towards biaxial fatigue crack growth tests and twin-disc tests featuring RCF crack growth. The framework has been employed to investigate the influence of the operational loads on the RCF crack path for a frictionless crack [4].

The current study enhances this development by investigating the effect of crack face friction. In the context of RCF of wheels and rails, crack face friction is affected by the penetration of lubrication (e.g., water or grease) into the RCF cracks. This will have the effect of lubricating the crack faces and thereby decreasing crack face friction. In addition, lubrication trapped in the crack may distribute pressure deeper into the crack and induce local pressurisation of the crack [5]. The effect of crack face friction on the shear loading of a crack subjected to rolling contact has been found to be significant [6]. Also, the combined influence of decreased friction and pressurisation on the crack load has been extensively investigated [7~9]. In short, pressurisation of the crack will tend to open the crack (mode I), which prevents crack face contact. In the case of a closed crack, decreased friction will facilitate the sliding of the crack faces (mode II). In general terms, the mode I load will tend to drive the crack in the direction that maximizes the opening of the crack, whereas the decreased friction will tend to promote sliding deformation and potential shear growth of the crack. What the combined result of these two effects regarding the direction of crack propagation will be is not straight-forward.

It has been shown in field tests [10] that water is indeed prone to penetrate surface initiated RCF cracks. However, for pressurisation to occur, the crack (or parts of it) also has to be fully sealed during the rolling contact. In a real wheel–rail contact where the cracking more relates to a network, see e.g. [11], this may be hard to achieve. Also, any pressurisation is likely confined to some parts of the cracks, and systematic analysis of this effect is challenging. For this reason, the current study focuses solely on the influence of crack face friction. In addition, the study leaves the fairly well-investigated field of crack loading and focuses solely on the direction of propagation of the cracks under varying loading conditions.

Experimental assessment of the frictional behaviour at crack faces in contact is inherently difficult, and the conditions in the field are even more difficult to measure. Therefore, the most basic Coulomb model, characterized by a single coefficient of friction, is adopted in this study to quantify the effect of friction.

The loading and deformation of propagating RCF cracks are evaluated using Finite Element (FE) simulations.

Thereby, the study presents an extension of [4], where propagation of cracks under operational conditions was considered for the frictionless case. Motivated by the findings in [2, 3], the direction of growth is predicted using an accumulated Vector Crack Tip Displacement (VCTD) criterion based on displacements extracted from linear elastic FE analyses. The qualitative influence of crack face friction on the RCF crack growth direction is obtained by comparing the predicted crack paths for frictional and frictionless cracks. Furthermore, an indication of the crack growth rate can be obtained by studying the ranges of the crack tip displacement components during a load cycle. In order to have a quantitative prediction of the RCF crack growth, model parameters must be further calibrated against experimental/field data.

2. Numerical framework

2.1. Model

Figure 1 shows a rectangular (rail) section with a width of $w = 300$ mm and height of $h = 100$ mm, which is taken to represent the rail domain in a 2D FE-model. The bottom side of the rail is restrained in the vertical direction ($u_y = 0$) and the side edge displacements are prescribed in the horizontal direction ($u_x = u_x^{\mathrm{p}}$).

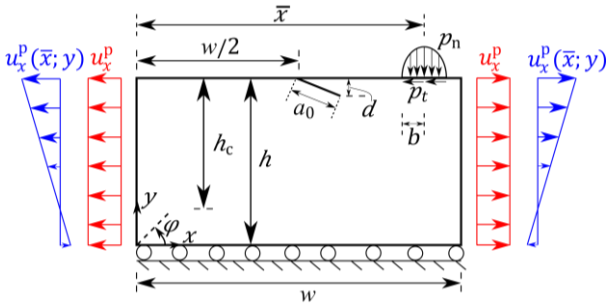

Figure 1 *A sketch of the 2D rail part with an inclined surface-breaking crack subjected to a Hertzian contact load (p_n, p_t) and constant longitudinal boundary displacements u_x^p (red), or, boundary displacements $u_x^p(\bar{x};y)$ pertinent to rail bending (blue).*

A surface-breaking inclined crack with the length of $a_0 = 4.3$ mm is considered in the rail in the direction of $\varphi_0 = -25°$ [12, 13], see Figure 1. The crack is modelled as a discrete crack. To apply the contact constraints at the crack faces in the normal and tangential directions, penalty formulations are employed. Coulomb friction is used in the constitutive equation where the tangential traction between two contacting surfaces, p_t, is evaluated as

$$\begin{cases} |p_t| \le \mu_{CF}\, p_n & v_t = 0 \text{ (stick condition)} \\ p_t = -\mu_{CF}\, p_n \frac{v_t}{|v_t|} & v_t \neq 0 \text{ (slip condition)} \end{cases}, \quad (1)$$

Here, v_t denotes the tangential (sliding) velocity, μ_{CF} and p_n are the friction coefficient, and the normal contact pressure at the contacting surfaces, respectively. The employed FE-mesh consists of linear triangular elements featuring ordinary elements with a size of 17 μm near the crack tip. The rail section is modelled with linearly elastic material under plane strain conditions. The modulus of elasticity and the Poisson's ratio of the rail material are taken as $E_r = 210$ GPa and $\nu_r = 0.3$, respectively.

2.2. Load scenarios

Cyclic loading of the rail is considered, and the rail part is subjected to three different load cases: wheel–rail contact load, rail bending load, and the thermal load, as described below.

2.2.1. Contact load

The wheel–rail contact loads consist of contact pressure and frictional stresses. The wheel–rail contact is modelled using Hertzian theory. The 2D contact pressure, p_n, has an elliptic distribution along the contact surface, which for a given wheel load position, $\bar{x}$, is expressed as [14]

$$p_n(\bar{x};x) = \begin{cases} \frac{2P}{\pi b^2}\sqrt{b^2 - [x-\bar{x}]^2} & |x-\bar{x}| < b \\ 0 & |x-\bar{x}| \ge b \end{cases}, \quad (2)$$

where P is the 2D contact load magnitude (per unit thickness) and $|\bullet|$ represents the absolute value. For a given load magnitude P, the semi-axis of the contact patch, b, is computed as

$$b = \sqrt{\frac{4PR}{\pi}\left(\frac{1-\nu_r^2}{E_r} + \frac{1-\nu_w^2}{E_w}\right)}. \quad (3)$$

Here, R is the radius of the wheel which is assumed to be 0.46 m and the elastic properties of the wheel material are taken as $E_w = 199$ GPa and $\nu_w = 0.3$.

It is presumed that frictional stresses in the wheel–rail interface follow the spatial distribution of the contact pressure (i.e. they are evaluated under an assumption of full slip) with a traction coefficient of f_{wr} which gives the frictional stress as $p_t(\bar{x};x) = f_{wr}\, p_n(\bar{x};x)$. A wheel passage is simulated by moving the contact load along the top surface of the rail. During pure contact loading, the vertical edges of the rail are clamped in the global x – direction ($u_x^p = 0$), see Figure 1.

2.2.2. Rail bending load

The rail bends as a wheel traverses the rail. To evaluate the bending moment, a 6 m section of the track with a rail profile of 60E1 subjected to a passing wheel load of 7.5 t with a velocity of 100 km/h has been considered. The crack mouth is assumed to be positioned midspan in between two adjacent sleepers. The evolution of the bending moment at the crack mouth in the presumed rail with the crack located at $\bar{x} = 0.15$ m is computed by the in-house vertical dynamic vehicle-track interaction analysis code, DIFF [15]. The final result is presented in Figure 2 [4]. To quantify the magnitude of the boundary displacements of the 2D rail section due to the rail bending load, it is assumed that the rail section is a beam that obeys the Euler-Bernoulli beam theory. Thus, the $u_x^p(\bar{x};y)$ is evaluated based on the moment–curvature relation for the presumed rail section using [16]

$$u_x^p(\bar{x};y) = \frac{M(\bar{x})\left[y - [h-h_c]\right]w}{2E_r I_z}, \quad (4)$$

where $M(\bar{x})$ is the bending moment at the wheel load position, $\bar{x}$, evaluated from Figure 2, w is the length of the rail section, $h_c = 0.091$ m and $I_z = 30.5\times 10^{-6}$ m^4 are the distance from the top surface of the rail to the

neutral axis, see Figure 1, and the second area moment of the rail profile [17], respectively.

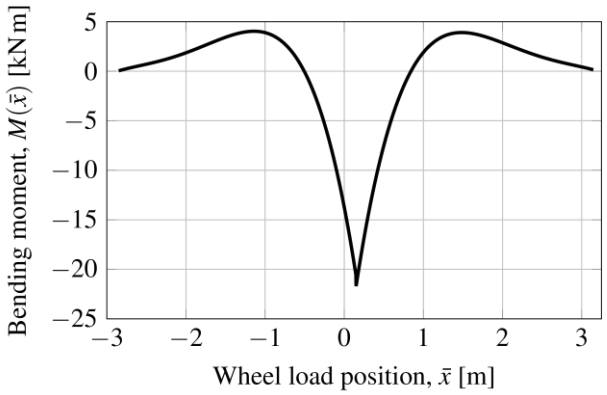

Figure 2 *Evolution of bending moment at the position of crack mouth as a function of the relative position of the wheel. Results from the vehicle-track simulation software DIFF [15].*

2.2.3. Thermal load

Thermal stresses in rail result from restricted thermal contractions due to ambient temperature variations ΔT from the stress-free temperature. These longitudinal stresses along the rail can be quantified using a linear thermoelasticity assumption. More precisely, approximating the rail as homogeneous and perfectly confined in the axial direction, the corresponding boundary displacements are [16]

$$u_x^{\mathrm{p}} = -\alpha_{\mathrm{r}} \Delta T w/2. \tag{5}$$

Here, $\alpha_{\mathrm{r}} = 11.5\times 10^{-6}$ [1/°C] is the coefficient of thermal expansion for the rail material and w is the length of the rail section.

2.3. Crack propagation criterion

The VCTD criterion proposed in [2] was developed based on the criterion suggested in [18] and modified to account for out-of-phase loading. It is utilized to predict crack growth direction for cyclic loading. The criterion employs the relative crack face deformations in the normal and tangential directions, $\delta_{\mathrm{I}}(t)$ and $\delta_{\mathrm{II}}(t)$ respectively, as shown in Figure 3b and postulates that the final crack growth direction for the presumed load cycle is in the direction of the crack driving displacement vector. For completion, the numerical procedure of the criterion [2] is briefly described below based on [4]:

1. $\delta_{\mathrm{I}}(t)$ and $\delta_{\mathrm{II}}(t)$ are computed at each time instance t of the load cycle at a constant distance, d_{h}, from the crack tip, see Figure 3. In this study, $d_{\mathrm{h}} \approx 52\ \mu$m was used.
2. To reflect kinematic hardening effects due to local plasticity at the crack tip, the 'amplitudes' of the crack face deformations, $\tilde{\delta}_{\mathrm{I/II}}(t)$, are employed here. Using $\bar{\delta}_{\mathrm{I/II}} = \frac{1}{2}\left[\max_t(\delta_{\mathrm{I/II}}(t)) + \min_t(\delta_{\mathrm{I/II}}(t))\right]$ as mid-values over the load cycle, 'amplitudes' of $\delta_{\mathrm{I}}(t)$ and $\delta_{\mathrm{II}}(t)$ are defined as

$$\tilde{\delta}_{\mathrm{I/II}}(t) = \delta_{\mathrm{I/II}}(t) - \bar{\delta}_{\mathrm{I/II}}. \tag{6}$$

3. Similar to [18], the instantaneous crack growth direction, $\vartheta(t)$, in the crack local coordinate system shown in Figure 3a, and the instantaneous crack driving displacement, $\tilde{\delta}(t)$, are introduced as[1]

$$\vartheta(t) = \arcsin\left(\frac{\tilde{\delta}_{\mathrm{II}}(t)}{\tilde{\delta}(t)}\right) \quad , \tag{7}$$

and

$$\tilde{\delta}(t) = \sqrt{\langle\tilde{\delta}_{\mathrm{I}}(t)\rangle^2 + 2\langle\tilde{\delta}_{\mathrm{I}}(t)\rangle\left|\tilde{\delta}_{\mathrm{II}}(t)\right| + 2\tilde{\delta}_{\mathrm{II}}(t)^2}\,. \tag{8}$$

4. Two trial crack driving displacements, $\Delta\mathbf{a}^+$ and $\Delta\mathbf{a}^-$, are defined to evaluate the tendency of the crack to propagate in the presumed positive and negative directions. These are based on the 'rate-independent' response over the entire load cycle. At the end of the load cycle, the trial crack driving displacement with the largest Euclidean norm is chosen as the final crack driving displacement using

$$\Delta\mathbf{a} = \underset{\Delta\tilde{\mathbf{a}}\in\{\Delta\mathbf{a}^+,\,\Delta\mathbf{a}^-\}}{\operatorname{argmax}} \|\Delta\tilde{\mathbf{a}}\|. \tag{9}$$

In this equation,

$$\Delta\mathbf{a}^{+/-} = \int_0^{T_{\mathrm{c}}} \boldsymbol{\delta}\mathbf{a}^{+/-}(\mathrm{t})\mathrm{d}t \quad , \qquad \boldsymbol{\delta}\mathbf{a}^{+/-}(\mathrm{t}) = \langle\frac{\mathrm{d}\tilde{\delta}(t)}{\mathrm{d}t}\rangle\,\hat{\boldsymbol{e}}_{\vartheta} f^{+/-}(\mathrm{t}) \quad , \tag{10}$$

where T_{c} denotes the duration of the presumed load cycle, and $\hat{\boldsymbol{e}}_{\vartheta}$ is the unit vector in the direction of the $\vartheta(t)$, evaluated from Eq. (7). Lastly,

$$f^+(\mathrm{t}) = \begin{cases} 0 & \tilde{\delta}_{\mathrm{II}}(t) < 0 \text{ and } \frac{\delta_{\mathrm{I}}(t)}{|\delta_{\mathrm{II}}(t)|} \le \psi \\ 1 & \tilde{\delta}_{\mathrm{II}}(t) \ge 0 \text{ or } \frac{\delta_{\mathrm{I}}(t)}{|\delta_{\mathrm{II}}(t)|} > \psi \end{cases}, \qquad f^-(\mathrm{t}) = \begin{cases} 0 & \tilde{\delta}_{\mathrm{II}}(t) > 0 \text{ and } \frac{\delta_{\mathrm{I}}(t)}{|\delta_{\mathrm{II}}(t)|} \le \psi \\ 1 & \tilde{\delta}_{\mathrm{II}}(t) \le 0 \text{ or } \frac{\delta_{\mathrm{I}}(t)}{|\delta_{\mathrm{II}}(t)|} > \psi \end{cases}, \tag{11}$$

where ψ is the reversed shear threshold parameter that can control the contribution of the time instances with reversed shear deformations[2]. More specifically, ψ relates to the required crack opening to allow for reversed shear contribution to the propagation during one cycle. For closed cracks, only the shear in the dominating/assumed direction of growth contributes to propagation. More detailed information on the influence of the ψ was presented in [4].

5. The final crack propagation direction at the end of the load cycle, ϕ, is defined by the following unit vector in the crack tip local coordinate system, see Figure 3a, as

$$\hat{\boldsymbol{e}}_{\phi} = \frac{\Delta\mathbf{a}}{\|\Delta\mathbf{a}\|} \quad . \tag{12}$$

[1] $\langle\bullet\rangle$ denotes the Macaulay brackets, $\langle\bullet\rangle = \frac{1}{2}\,[\bullet + |\bullet|]$.

[2] In this study, reversed shear deformations are defined as shear deformations of the crack which are in the opposite direction to the assumed direction of the trial crack driving displacement.

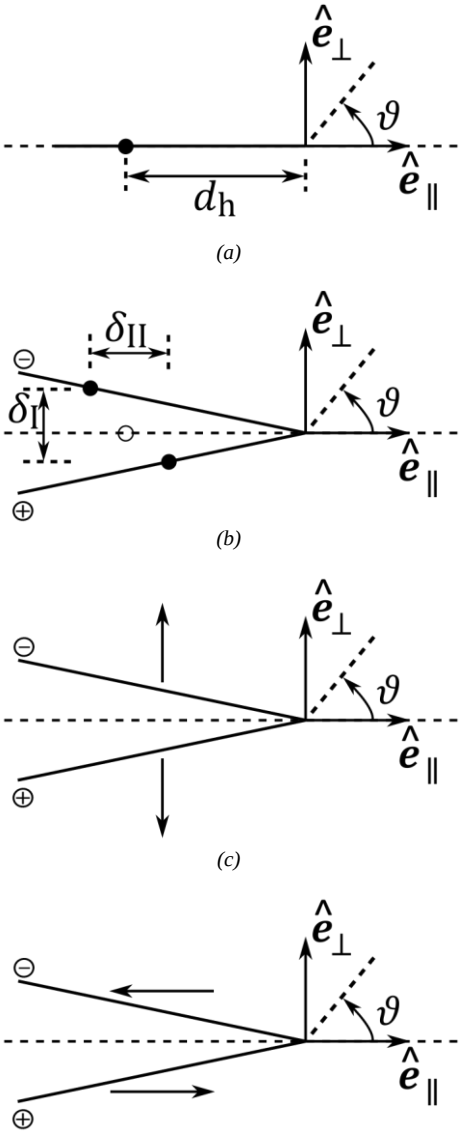

Figure 3 *Crack geometry configurations. Dashed lines indicate the orientation of the undeformed crack. (a) Undeformed closed crack. (b) Crack face displacements. (c) Illustration of positive crack opening, δ_I. (d) Illustration of positive crack sliding, δ_{II}.*

2.4. Simulation of crack propagation

Each load cycle is simulated in the FE analysis. The crack growth direction is predicted using the accumulative VCTD criterion described in Section 2.3. The accumulated growth for considering multiple cycles is simulated by propagating the discrete crack in the predicted direction and repeating the process for each cycle.

In this study, the rate of propagation is not predicted. Therefore, the length of the incremental propagation of the crack is a pure discretisation parameter (rather than representing a certain number of load cycles).

3. Analyses and results

The FE-model detailed in Section 2.1 subjected to the three different load scenarios of pure contact load, combined thermal and contact loads, and combinations of bending and contact load, as described in Section 2.2, was implemented in ABAQUS/CAE [19]. The crack growth direction was evaluated based on the accumulated VCTD criterion outlined in Section 2.3 by post-processing the resolved displacement field in MATLAB [20]. Finally, the crack was propagated in an unbiased fashion in the predicted direction with a growth increment of 0.2 mm, as discussed in Section 2.4. Crack paths presented in the following subsections were evaluated during three growth increments. The maximum value of the crack face penetration obtained in the FE-simulations was below 0.06 μm. Also, the ranges of the crack face deformations, $\Delta\delta_I$ and $\Delta\delta_{II}$, were used as an indication to compare the crack growth rate qualitatively for the considered load scenarios. Here, the deformation ranges for the initial crack were employed to remove any effects of crack geometry.

3.1. Pure contact load

A pure contact load magnitude of $P = 33.8$ MN/m with a traction coefficient of $f_{wr} = 0.3$ was applied to the FE-model shown in Figure 1 with $u_x^p = 0$. According to Eq. (3), the semi-axis of the contact patch was $b =$ 13.3 mm. In order to investigate the influence of the crack face friction on the crack growth, the predicted crack path and the ranges of crack face displacements for a crack with a crack face friction coefficient of $\mu_{CF} = 0$, $\mu_{CF} = 0.3$ and $\mu_{CF} = 0.5$ are presented in Figure 4 and Table 1, respectively. It is expected that friction truncates the crack shear deformations while not having any influence on the crack opening. Hence, a crack with high crack face friction should have a higher share of mode I loading, and should grow into the rail with less deviation from the initial crack, i.e. more towards mode I growth, in comparison to the frictionless crack. Figure 4 reflects this expectation with minor differences between frictional cracks with $\mu_{CF} = 0.3$ and $\mu_{CF} = 0.5$. Table 1 indicates that the crack face friction does not have an influence on the crack opening but reduces crack sliding. Thus, the crack growth rate can be expected to be slower as crack face friction increases.

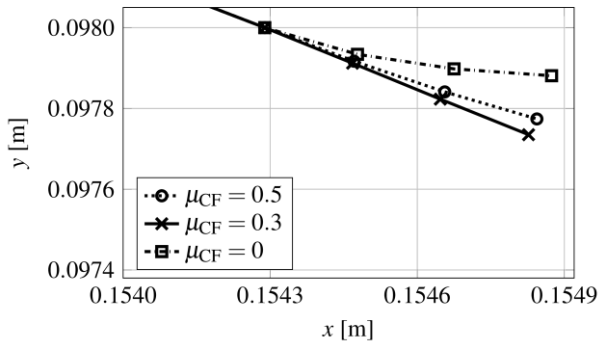

Figure 4 *Predicted crack paths for frictional crack with $\mu_{CF} = 0.3$ and $\mu_{CF} = 0.5$ and frictionless crack ($\mu_{CF} = 0$) under pure contact load with $P = 33.8$ MN/m, $f_{wr} = 0.3$ and $\psi = 0.01$.*

Table 1 *Influence of the crack face friction coefficient, μ_{CF}, on the ranges of the crack face displacements, $\Delta\delta_I$ and $\Delta\delta_{II}$, for the initial crack under pure contact load with $P = 33.8$ MN/m and $f_{wr} = 0.3$.*

μ_{CF} [−]	$\Delta\delta_I$ [μm]	$\Delta\delta_{II}$ [μm]
0	1.66	7.55
0.3	1.66	5.69
0.5	1.66	4.66

3.2. Combined thermal and contact load

Boundary displacements, u_x^{p}, corresponding to $\Delta T = -20$ °C from Eq. (5) were applied to the model depicted in Figure 1 in combination with a contact load at two different magnitudes of $P = 7.3$ MN/m and $P = 33.8$ MN/m with $f_{\mathrm{wr}} = 0.3$. The crack face friction coefficient was set to $\mu_{\mathrm{CF}} = 0.3$. Figure 5 demonstrates the predicted crack paths for these load combinations. It shows that the crack subjected to a combined loading tends to grow shallower than under pure contact load. This is not in line with the observations for a frictionless crack in [4], where gradual changes in the crack path from pure thermal to pure contact load were predicted. There are two possible reasons for this behaviour. It can be the influence of the mid-value ($\bar{\delta}$) correction (explained below), or an influence of the reversed shear condition employed in the criterion.

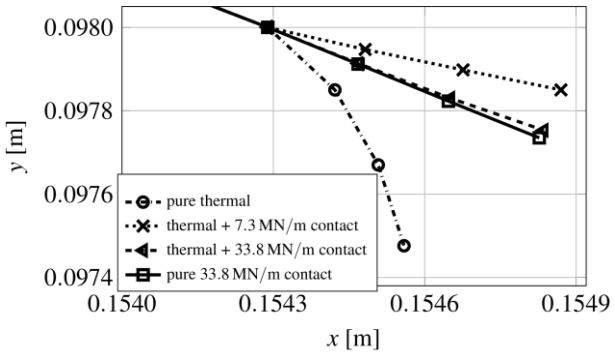

Figure 5 *Predicted crack paths for a frictional crack with $\mu_{\mathrm{CF}} = 0.3$ under combined thermal and contact loads with $f_{\mathrm{wr}} = 0.3$ for $\psi = 0.01$.*

In operations, the length of the temperature load cycle, being on the order of hours or days, is much longer than the contact load cycle, which is on the order of milliseconds. Thus, several contact load cycles can occur within a certain temperature load cycle and the kinematic hardening effects at the crack tip thus mainly pertain to the contact load part for each load cycle. To consider this effect in the simulations, $\bar{\delta}$ is calculated based solely on the pure contact load part of each combination (henceforth denoted $\bar{\delta}$-correction) and the pertinent results are presented in Figure 6. The predicted crack path for thermal and 33.8 MN/m contact load using $\bar{\delta}$-correction shows an expected behaviour based on the results from the frictionless crack, cf. [4]. The exception is the crack path for thermal and 7.3 MN/m contact load, which initially tends to grow deeper than for pure thermal load and has a 'jagged' path. This behaviour can be the influence of truncating contributions of the reversed shear instances since these should promote a shallower growth in general, and in particular in the first load increment.

In order to investigate the influence of the reversed shear contributions in the criterion, the reversed shear condition is removed to reflect the extreme case. Hence, Eq. (10) of the criterion detailed in Section 2.3 can be presented as

$$\Delta\mathbf{a} = \int_0^{T_{\mathrm{c}}} \boldsymbol{\delta}\mathbf{a}(\mathrm{t})\mathrm{d}t \quad , \qquad \boldsymbol{\delta}\mathbf{a}(\mathrm{t}) = \langle \frac{\mathrm{d}\tilde{\delta}(t)}{\mathrm{d}t} \rangle \, \hat{\boldsymbol{e}}_{\vartheta} \quad , \qquad (13)$$

which is equivalent to consider a negative value for the ψ parameter in the formulation of the criterion in Section 2.3.

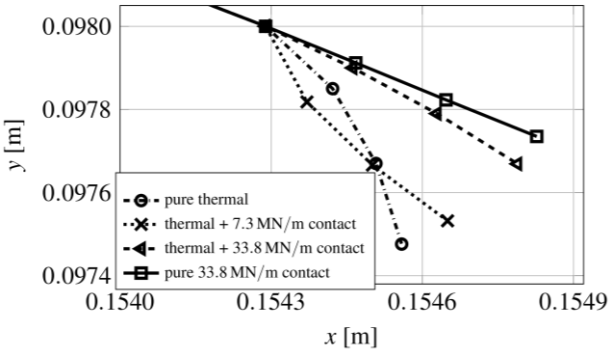

Figure 6 *Predicted crack paths with $\bar{\delta}$-correction for a frictional crack with $\mu_{\mathrm{CF}} = 0.3$ under combined thermal and contact loads with $f_{\mathrm{wr}} = 0.3$ for $\psi = 0.01$.*

Figure 7 shows the predicted crack paths when neglecting reversed shear condition and considering the $\bar{\delta}$-correction. Comparing Figure 6 and frictional paths in Figure 7, it is seen that the 'jagged' path observed in Figure 6 for thermal and 7.3 MN/m contact load is eliminated.

Regarding the influence of the crack face friction on the predicted crack path, the trend of the results in Figure 7 is the same for the frictional and frictionless paths with a little more deviation towards transverse growth for the thermal and 7.3 MN/m contact load in the case of a frictionless crack. This can be reasonable due to the fact that the frictionless crack should deviate more towards the shearing mode. Note that, since the reversed shear condition is neglected in the predicted paths shown in Figure 7, the pure contact paths differ a bit from what is shown in Figure 4. Based on Figure 7, it is concluded that the crack face friction has a moderate influence on predicted crack path.

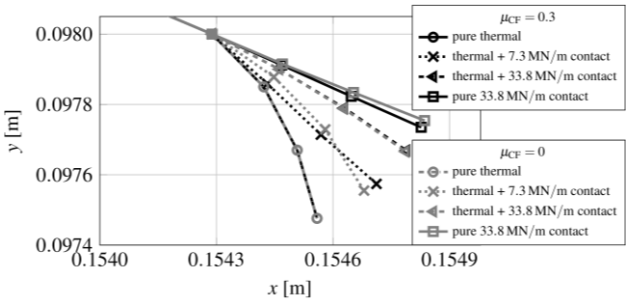

Figure 7 *Comparison of predicted crack paths under combined thermal and contact loads with $f_{\mathrm{wr}} = 0.3$ for frictional ($\mu_{\mathrm{CF}} = 0.3$) and frictionless crack, neglecting the reversed shear condition and employing $\bar{\delta}$-correction.*

The ranges of crack face displacements for the initial crack under the considered combined loads are tabulated in Table 2. Similar to the case of a pure contact load, crack face friction can be expected to reduce the crack growth rate since it reduces the crack face shear deformation (while having no influence on crack opening). Moreover, it is observed that the ranges for case of a thermal and a 7.3 MN/m contact load is higher than for the pure thermal loading, and that the combination of thermal and 33.8 MN/m contact load is higher than a pure 33.8 MN/m contact load. This is to be expected as a

reflection of the increased loading.

Table 2 *Influence of the crack face friction coefficient, μ_{CF}, on the ranges of the crack face displacements, $\Delta\delta_I$ and $\Delta\delta_{II}$, for the initial crack under combined thermal and contact load with $f_{wr} = 0.3$.*

load type	μ_{CF} [−]	$\Delta\delta_I$ [μm]	$\Delta\delta_{II}$ [μm]
pure thermal	0	0.24	0.18
thermal + 7.3 MN/m contact	0	0.66	3.16
thermal + 33.8 MN/m contact	0	1.90	7.55
pure 33.8 MN/m contact	0	1.66	7.55
pure thermal	0.3	0.24	0.18
thermal + 7.3 MN/m contact	0.3	0.66	2.30
thermal + 33.8 MN/m contact	0.3	1.90	5.82
pure 33.8 MN/m contact	0.3	1.66	5.69

3.3. Combinations of bending and contact load

The model illustrated in Figure 1 was loaded by boundary displacements pertinent to the bending load described by $u_x^p(\bar{x}; y)$ in Eq. (4). In addition, Hertzian contact loads of three different magnitudes: $P = 7.3$ MN/m, $P = 14.0$ MN/m and $P = 33.8$ MN/m were applied. The traction and crack face friction coefficients were taken as $f_{wr} = 0.3$ and $\mu_{CF} = 0.3$, respectively. The predicted crack paths under the combined loads are shown in Figure 8. Although the general trend is close to predictions for a frictionless cracks presented in [4], two discrepancies are found. The combination of bending and 33.8 MN/m contact load results in a shallower path than the pure contact load, and the crack path for the combination of bending and 7.3 MN/m is slightly 'jagged' although the crack deviates less from the previous crack segment when the crack propagates, i.e. the share of the mode I in the crack loading is increasing.

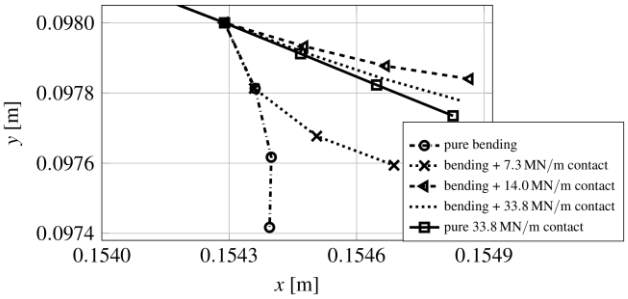

Figure 8 *Predicted crack paths for a crack with a friction coefficient of $\mu_{CF} = 0.3$ under combinations of bending and contact load with $f_{wr} = 0.3$ for $\psi = 0.01$.*

The $\bar{\delta}$-correction, explained in Section 3.2, is not applicable to this load combination since the load cycle length of bending and contact are on the same order. Hence, what remains to investigate compared to the previous section is the influence of the reversed shear condition in the criterion. As an extreme case, similar to that for the study in Section 3.2, the reversed shear condition is neglected in the criterion, and results are presented in Figure 9. The predictions show a gradual change in predicted crack paths from the pure bending load to a pure contact load. Also, it is observed that the 'jagged' path for the combination of bending and 7.3 MN/m contact load is eliminated when eliminating the reversed shear restrictions. Comparing the predicted crack paths in Figure 9 shows that a crack with crack face friction is predicted to grow deeper into the rail than a frictionless crack.

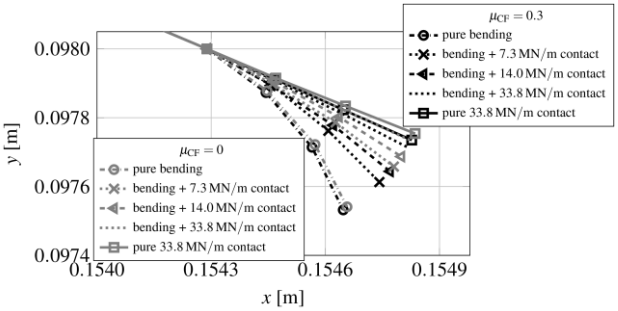

Figure 9 *Comparison of predicted crack paths under combinations of bending and contact load neglecting the reversed shear condition with $f_{wr} = 0.3$.*

Table 3 shows that the crack growth rate for a crack with crack face friction can be expected to be lower than for a frictionless crack under combinations of bending and contact load due to the decreased shear deformation. Furthermore, the crack can be expected to grow faster than for pure bending when it is subjected to combined loading due to the overall larger loads acting on the crack. However, for this load case, the combination of bending and a 33.8 MN/m contact load can be expected to result in a slower crack propagation than a pure contact load. This is due to the large compressive loading from bending that closes the crack as the contact load passes, see Figure 2.

Table 3 *Influence of the crack face friction coefficient, μ_{CF}, on the ranges of the crack face displacements, $\Delta\delta_I$ and $\Delta\delta_{II}$, for the initial crack under combinations of bending and contact load with $f_{wr} = 0.3$.*

load type	μ_{CF} [−]	$\Delta\delta_I$ [μm]	$\Delta\delta_{II}$ [μm]
pure bending	0	0.03	0.22
bending + 7.3 MN/m contact	0	0.25	3.16
bending + 14.0 MN/m contact	0	0.61	4.63
bending + 33.8 MN/m contact	0	1.49	7.55
pure 33.8 MN/m contact	0	1.66	7.55
pure bending	0.3	0.03	0.19
bending + 7.3 MN/m contact	0.3	0.25	2.11
bending + 14.0 MN/m contact	0.3	0.61	3.23
bending + 33.8 MN/m contact	0.3	1.49	5.61
pure 33.8 MN/m contact	0.3	1.66	5.69

4. Conclusions and outlook

A numerical procedure for simulating RCF crack growth under operational load scenarios while accounting for crack face friction has been developed. An isolated surface-breaking inclined crack is included in a 2D representation of the rail. The numerical model features linear elastic material and plane strain conditions. The crack face friction is included using the Coulomb friction model, and the crack growth direction has been evaluated from an accumulative VCTD criterion. It was shown that frictional cracks under pure contact loading tend to grow deeper into the rail in comparison to frictionless cracks.

Results from simulations of combined contact load and bending or thermal loading identified the need to reconsider some of the adopted parameter values in the VCTD criterion. By applying a $\bar{\delta}$-correction and neglecting the reversed shear condition previously employed in the criterion, a gradual transition in the predicted crack path from pure thermal to pure contact load conditions was observed as the contact load magnitudes were increased. For this load combination,

friction had a moderate influence on the predicted crack paths. A trend of gradual change between the pure load cases was also obtained for predicted crack paths under combinations of bending and contact load when the reversed shear condition was neglected. Similar to the case of a pure contact load, a frictional crack was predicted to propagate deeper into the rail.

A qualitative indication of crack growth rate based on the range of the crack face displacements close to the crack tip was also investigated. It was concluded that crack face friction can be expected to slow down the crack growth rate for all of the considered load cases by reducing the crack sliding range. In contrast, the crack opening is not affected (as expected).

The above conclusions were drawn based on a limited number of investigated loading scenarios. A parametric study on the influence of different modelling and loading parameters will improve the understanding of sensitivities and limitations of the developed numerical procedure. The full verification of 2D model predictions under operational loading scenarios is complex due to a scale difference between the model (2D) and the measured data (3D) and the issues associated with scale difference such as transferring the 3D contact load and crack geometry to 2D, mapping the 3D crack path into 2D, etc. This can be even harder when friction is considered, since measuring crack face friction in experiment/field tests is not straightforward.

Verification towards experimental results/field data has therefore not been considered in this research, although the predictive model has previously been validated towards more controlled biaxial (tensile) tests [2]. In the extension, 3D modelling of the rail would allow for better quantitative verification since scaling and mapping issues would be resolved. However, this would require an extension of the current criterion for crack growth since a crack front will have to be considered. In the current study, it has been shown that the predicted crack path using the developed procedure is sensitive to employed values of parameters in the criterion and the computational procedure. Hence, special attention needs to be observed in the calibration of the model towards experimental results/field data.

Finally, it can be observed that the loading of RCF cracks is non-proportional. This significantly complicates predictions of crack growth rates. Since a full verification of the predictive model has to include crack growth rate predictions, this is an issue that requires attention.

Acknowledgements

The current study is part of the ongoing activities in CHARMEC – Chalmers Railway Mechanics (www.chalmers.se/charmec). Parts of the study have been funded from the European Union's Horizon 2020 research and innovation programme in the project In2Track3 under grant agreement No 101012456.

References

[1] E.E. Magel: *Rolling contact fatigue: A comprehensive review*, US Department of Transportation: Federal Railroad Administration, 2011.

[2] D. Floros, A. Ekberg and F. Larsson: *Evaluation of crack growth direction criteria on mixed-mode fatigue crack growth experiments*, International Journal of Fatigue, 2019, 129 105075.

[3] D. Floros, A. Ekberg and F. Larsson: *Evaluation of mixed-mode crack growth direction criteria under rolling contact conditions*, Wear, 2020, 448-449 203184.

[4] M. Salahi Nezhad, D. Floros, F. Larsson, E. Kabo and A. Ekberg: *Numerical predictions of crack growth direction in a railhead under contact, bending and thermal loads*, Engineering Fracture Mechanics, 2022, 261 108218.

[5] A.F. Bower: *The Influence of Crack Face Friction and Trapped Fluid on Surface Initiated Rolling Contact Fatigue Cracks*, Journal of Tribology, 1988, 110(4) 704-711.

[6] A.D. Hearle and K.L. Johnson: *Mode II stress intensity factors for a crack parallel to the surface of an elastic half-space subjected to a moving point load*, Journal of the Mechanics and Physics of Solids, 1985, 33(1) 61-81.

[7] S. Bogdański, M. Olzak and J. Stupnicki: *Numerical stress analysis of rail rolling contact fatigue cracks*, Wear, 1996, 191(1) 14-24.

[8] S. Bogdański and M.W. Brown: *Modelling the three-dimensional behaviour of shallow rolling contact fatigue cracks in rails*, Wear, 2002, 253(1) 17-25.

[9] S. Bogdański, P. Lewicki and M. Szymaniak: *Experimental and theoretical investigation of the phenomenon of filling the RCF crack with liquid*, Wear, 2005, 258(7) 1280-1287.

[10] D.I. Fletcher, P. Hyde and A. Kapoor: *Modelling and full-scale trials to investigate fluid pressurisation of rolling contact fatigue cracks*, Wear, 2008, 265(9) 1317-1324.

[11] K.A. Meyer, D. Gren, J. Ahlström and A. Ekberg: *A method for in-field railhead crack detection using digital image correlation*, International Journal of Rail Transportation, 2022. doi:10.1080/23248378.2021.2021455

[12] R. Heyder and G. Girsch: *Testing of HSH® rails in high-speed tracks to minimise rail damage*, Wear, 2005, 258(7-8) 1014-1021.

[13] R. Stock and R. Pippan: *RCF and wear in theory and practice—The influence of rail grade on wear and RCF*, Wear, 2011, 271(1-2) 125-133.

[14] K.L. Johnson: *Contact Mechanics*, Cambridge University Press, 1985.

[15] J.C.O. Nielsen and A. Igeland: *Vertical dynamic interaction between train and track influence of wheel and track imperfections*, Journal of Sound and Vibration, 1995, 187(5) 825-839.

[16] S.P. Timoshenko and J.N. Goodier: *Theory of Elasticity*, McGraw-Hill, 1951.

[17] *CEN Railway applications - Track - Rail - Part 1: Vignole railway rails 46 Kg/m and above. EN 13674-1:2011*, European Committee for

Standardization, 2011.
[18] C. Li: *Vector CTD criterion applied to mixed mode fatigue crack growth*, Fatigue & Fracture of Engineering Materials & Structures, 1989, 12(1) 59-65.
[19] *ABAQUS/Standard User's Manual, Version 2020*, Dassault Systèmes Simulia Corp., 2020.
[20] *MATLAB 9.7.0.1190202 (R2019b)*, The MathWorks Inc., 2019.